# Durham Research Online

## Deposited in DRO:

16 May 2018

## Version of attached file:

Accepted Version

## Peer-review status of attached file:

Peer-reviewed

## Citation for published item:

Magnier, E.A. and Tonry, J.L. and Finkbeiner, D. and Schlafly, E. and Burgett, W.S. and Chambers, K.C. and Flewelling, H.A. and Hodapp, K.W. and Kaiser N., N. and Kudritzki, R.-P. and Metcalfe, N. and Wainscoat, R.J. and Waters, C.Z. (2018) 'Charge diffusion variations in Pan-STARRS1 CCDs.', Publications of the Astronomical Society of the Pacific., 130 (988). 065002.

## Further information on publisher's website:

## Publisher's copyright statement:

## Additional information:

# Charge Diffusion Variations in Pan-STARRS 1 CCDs

Eugene A. Magnier,[1] J. L. Tonry, [1] D. Finkbeiner,[2] E. Schlafly,[3,4] W. S. Burgett,[1] K. C. Chambers,[1] H. A. Flewelling,[1] K. W. Hodapp,[1] N. Kaiser,[1] R.-P. Kudritzki,[1] N. Metcalfe,[5] R. J. Wainscoat,[1] and C. Z. Waters,[1]

## ABSTRACT

Thick back-illuminated deep-depletion CCDs have superior quantum efficiency over previous generations of thinned and traditional thick CCDs. As a result, they are being used for wide-field imaging cameras in several majorxs projects. We use observations from the Pan-STARRS $3\pi$ survey to characterize the behavior of the deep-depletion devices used in the Pan-STARRS 1 Gigapixel Camera. We have identified systematic spatial variations in the photometric measurements and stellar profiles which are similar in pattern to the so-called "tree rings" identified in devices used by other wide-field cameras (e.g., DECam and Hypersuprime Camera). The tree-ring features identified in these other cameras result from lateral electric fields which displace the electrons as they are transported in the silicon to the pixel location. In contrast, we show that the photometric and morphological modifications observed in the GPC1 detectors are caused by variations in the vertical charge transportation rate and resulting charge diffusion variations.

*Subject headings:* Surveys:Pan-STARRS 1

## 1. INTRODUCTION

CCD detectors have evolved greatly since they were first introduced for astronomical imaging in the mid 1970s. In addition to the well-known increases in the size of CCDs over the past 4 decades, CCD architecture has gone through three major evolutionary stages.

The first generation of CCDs used a silicon substrate a few hundred microns thick on top of which gate structures were deposited to define the pixels. A positive voltage applied to the gate layers would create a shallow region ($\sim$10 microns thick) in which the holes were depleted. This "depletion region" acted as a potential well to trap electrons, specifically those generated by absorbed photons. The thick silicon substrate required illumination from the "front" side containing the thin gate structures to allow the photons to reach the depletion region and be detected. These early CCDs had modest quantum efficiency as photons were easily absorbed by the several-micron-thick gate structures. For an excellent review of the history of CCD development, see Janesick & Elliott (1992).

Thinned, backside-illuminated CCDs such as the TI 3PCCD (Blouke et al. 1981) were developed to address the quantum efficiency limitations of the first generation thick CCDs. The silicon substrate was

---

[1]Institute for Astronomy, University of Hawaii, 2680 Woodlawn Drive, Honolulu HI 96822

[2]Harvard-Smithsonian Center for Astrophysics, 60 Garden Street, Cambridge, MA 02138

[5]Department of Physics, Durham University, South Road, Durham DH1 3LE, UK

[3]Lawrence Berkeley National Laboratory, One Cyclotron Road, Berkeley, CA 94720, USA

[4]Hubble Fellow

removed using a chemical process, leaving a delicate device only $\sim$10 - 20$\mu$m thick, exposing the depletion region on the backside. Photons entering the backside of the device are not blocked by the gate structures and are thus more easily absorbed and detected. Thinned backside-illuminated CCDs have high quantum efficiency to blue photons. However, as the wavelength increases beyond $\sim$800 nm, the silicon becomes more transparent to the photons with a corresponding drop in quantum efficiency for red photons. In addition, thin-film interference between the entering photons and those reflecting off the front side of the CCD result in "fringe" patterns for redder photons.

Early generations of CCDs were made of low-resistivity ($\sim$10 - 50 $\Omega$-cm) silicon. Following experiments beginning in the early 1990s (Holland et al. 1996), CCDs made from thick, high-resistivity ($> 10k\Omega$-cm) silicon were developed for astronomical instruments in the early 2000s (Holland et al. 2003). The high-resistivity of the silicon allows for depletion regions of hundreds of microns in depth, compared to $\sim$10$\mu$m for the low-resistivity silicon. This modification allows for a back-illuminated CCD with a relatively thick silicon subtrate of 75 - 300$\mu$m. Blue photons impinging on the back of the device are absorbed near the back surface of the device and are caried through the depletion region to the gates on the front side. The thick silicon allows red photons to have a greater chance to be absorbed, increasing quantum efficiency in the red. Because these thick, deep-depletion devices have near-unity quantum efficiency across a very wide spectral range, they have become the design of choice for many modern, large-scale CCD cameras (e.g., Pan-STARRS GPC1, Tonry & Onaka 2009; Subaru Hypersuprime Camera, Komiyama et al. 2010; Dark Energy Survey Camera, Flaugher et al. 2015).

While these deep-depletion CCDs seem to be ideal, they do have features which can cause challenges for precise measurements. For example, as a result of the "Brighter-Fatter Effect" (Antilogus et al. 2014; Gruen et al. 2015), the profile of bright stars are measured to be wider than the profiles of faint stars. The accepted interpretation is that the electric fields produced by the electrons accumulated from a star repel successive incoming electrons, with the repulsion increasing the more electrons have accumulated.

The effects of lateral electric fields are likewise identified as the cause of the so-called "tree rings" observed in the flat-field, astrometry, and photometry response of thick deep-depletion detectors (Plazas et al. 2014). These tree-ring patterns have been noted in the flat-field response of deep depletion devices since their early testing (see, e.g., Figure 2 in Estrada et al. 2010) and were initially considered to be a sensitivity response which could be removed with a flat-field. As discussed in detail by Plazas et al. (2014), these tree rings are more correctly interpretted as variations in the effective pixel area due to migration of the electrons pushed by lateral electric fields induced by small changes in the doping used to set the resistivity of the silicon. The changes in the effective area result in changes to the apparent flat-field response as well as the astrometric response of the detector. More subtly, the changes in the flat-field response, since they do not reflect actual variations in sensitivity, can lead to systematic photometry errors for astronomical sources if flat-field images are used in the standard fashion.

In this paper, we examine the behavior of an apparently-similar kind of tree-ring pattern observed in the Pan-STARRS 1 Gigapixel Camera 1 CCDs. Although we also observe the changes in effective pixel area caused by lateral electric fields as described by Plazas et al. (2014), we show below a second effect which is more important in these devices in driving systematic photometry errors. We find that variations in charge diffusion, also resulting from changes in the silicon doping structures, affect both the observed stellar profiles as well as the photometry measured with profile fitting techniques. In Section 2, we discuss the Pan-STARRS 1 telescope, camera, and survey data used in this analysis. In Section 3, we present the tree-ring patterns as observed in several different types of measurements: flat-field response, systematic photometric residuals, systematic astrometric residuals, and stellar profile shape variations. In Section 4,

we discuss the interpretation of patterns we observe and present a simple model to explain the observed behavior. We conclude with a discussion of the implications of this effect on astronomical measurements from deep depletion instruments

## 2. Pan-STARRS1

The 1.8m Pan-STARRS 1 telescope (PS1), located on the summit of Haleakala on the Hawaiian island of Maui, has been surveying the sky regularly since May 2010 (Chambers et al. 2017). From May 2010 through March 2014, PS1 was run under the aegis of the Pan-STARRS 1 Science Consortium (PS1SC) to perform a set of wide-field science surveys; since March 2014, operations have been supported primarily by NASA's Near Earth Object Observation program (see Wainscoat et al. 2015). Under the PS1SC, the largest survey, both in terms of area of the sky covered ($3\pi$ steradians) and fraction of observing time (56%), was the $3\pi$ Survey in which the entire sky north of Declination $-30°$ was imaged $\sim$80 times over 4 years. These observations were distributed over five filters, $g_{P1},r_{P1},i_{P1},z_{P1},y_{P1}$, and have been astrometrically and photometrically calibrated to good precision (Magnier et al. 2016a).

The wide-field PS1 telescope optics (Hodapp et al. 2004) image a 3.3 degree field of view on a 1.4 gigapixel camera (GPC1; Tonry & Onaka 2009), with low distortion and generally good image quality. The median seeing for the $3\pi$ Survey data vary somewhat by filter: $(g_{P1},r_{P1},i_{P1},z_{P1},y_{P1}) = (1.31, 1.19, 1.11, 1.07, 1.02)$ arcseconds. Routine observations are conducted remotely from the Advanced Technology Research Center in Kula, the main facility of the University of Hawaii's Institute for Astronomy operations on Maui.

GPC1, currently the largest astronomical camera in terms of number of pixels, consists of a mosaic of 60 edge-abutted $4800 \times 4800$ pixel detectors, with 10 $\mu$m pixels subtending 0.258 arcsec. These CCID58 detectors, manufactured by Lincoln Laboratory, are $75\mu$m-thick back-illuminated CCDs (Tonry et al. 2006, 2008). Initial performance assessments are presented in Onaka et al. (2008). The active, usable pixels cover $\sim$80% of the FOV.

### 2.1. Data Processing and Calibration

Images obtained by PS1 are processed by the Pan-STARRS Image Processing Pipeline (IPP; Magnier 2006; Magnier et al. 2017). All observations are processed nightly, with results sent to groups within the science consortium (i.e., PS1SC during the $3\pi$ Survey) performing short-term science projects (e.g., searching for transient and moving objects). In addition, the $3\pi$ Survey dataset has been re-processed several times with improved calibration and analysis techniques. To date (2017 September), 3 re-processings starting from raw pixel data have been performed. The labels PV0, PV1, PV2, PV3 are used identify the nightly processing and successive re-processing versions. PV3 has been used for the public release of the Pan-STARRS $3\pi$ Survey data via the *Barbara A. Mikulski Archive for Space Telescopes* (MAST) at the Space Telescope Science Institute.[1] The process of the construction of this database and the schema details are discussed in detail by Flewelling et al. (2016).

The data processing and calibration operations are discussed in detail in elsewhere (Magnier et al. 2016b,a; Waters et al. 2016). We re-visit here a number of points that are of significance to this study.

---

[1] http//panstarrs.stsci.edu

Images are processed following a fairly standard sequence of image detrending, source detection, and initial calibration (astrometric and photometric) of those detected sources. Additional standard processing critical to PS1 science operations includes geometric transformation ('warping') and image combinations (summed stacks and differences). For the purposes of this analysis, we are only considering the sources detected in the individual exposures from the initial analysis steps.

As discussed in Waters et al. (2016), image detrending includes flat-field processing with a single epoch flat-field image for each filter. The flat-field image used for this analysis has been generated by median-combining dome flat-field images (after pre-processing and pixel outlier rejections) and then multiplying by a photometric flat-field correction image generated by the analysis of a grid of images of a dense stellar field. The purpose of this second step is to correct the basic flat-field image for errors arising from the non-uniformity of the illumination, from non-pixel uniformity due to the varying optical distortion across the field, and any other factors which may make the flat-field image inconsistent with stellar photometry, e.g., SED, filter band-pass variations, etc (see Waters et al. 2016; Magnier & Cuillandre 2004; Magnier 2007). This correction was made on a relatively coarse grid across the focal plane in order to accumulate sufficient statistics from the stars in the relatively small number of images available at the time. We have found that a single flat-field set can be used for all PS1 observations to yield photometric systematic errors at the level of $\sim2\%$. PS1 benefits in this regard from the stability of having a single instrument which is rarely removed.

Photometry of the PS1 images is performed using a point-spread-function (PSF) model as well as multiple kinds of apertures (Magnier et al. 2016b). In this analysis, we refer to aperture photometry performed using an aperture defined based on the image quality observed for a given chip. The aperture diameter is set to be 3.75 times the FWHM for the image.

To improve the photometric systematic errors beyond the level achieved with a single (photometrically corrected) flat-field set, the PS1 photometry is re-calibrated within the databasing system based on the properties of the measured photometry. The calibration process is discussed by Schlafly et al. (2012) and Magnier et al. (2013, 2016a). As part of this process, several flat-field corrections have been determined. For the PV2 analysis discussed here, a flat-field correction determined during the ubercal analysis (see Schlafly et al. 2012) consisted of an $8 \times 8$ grid of corrections for each GPC1 chip, corresponding to a correction for each OTA "cell" and filter for each of 4 seasons. The boundaries of those seasons are tentatively identified with modifications to the baffle structures or the system optics. The critical point here is that the final effective flat-field image for the PV2 dataset is based on a dome-flat at the highest resolution, with very low resolution (hundreds of pixels) corrections based on photometry, resulting in photometric systematic uncertainties in the range 7 - 12 millimagnitudes, depending on the filter (Magnier et al. 2013).

For all objects, positions are measured from the PSF model for the brighter sources (using a non-linear fitting process) and from a simple centroid (1st moment) for the fainter source (Magnier et al. 2016b). These position measurements are used in the astrometric analysis. The astrometric calibration is discussed by Magnier et al. (2016a); for the PV2 dataset, the typical systematic floor is $\sim$15 - 20 milliarcsecond for individual measurements of brighter stars.

## 3. Tree-Ring Patterns

For many of the GPC1 OTA CCDs, we observe a spatial pattern in the photometric residuals for each device which is similar in appearence to the tree rings described in the Dark Energy Camera (DECam) by Plazas et al. (2014). This pattern consists of systematic deviations which are consistent in a set of circular

arcs centered on the corner of the CCD, as shown in Figure 1. The details of the analysis used to generate Figure 1 are given below. For now, we note that the GPC1 CCDs are constructed by dividing the circular silicon wafer into 4 inscribed squares. Thus the corners of the CCDs lie in the center of the silicon boule, just as the center of the circular tree rings described by Plazas et al. (2014) match the center of the boule from which they came. This gives the impression that a similar mechanism is responsible for the pattern observed in the PS1 photometry and the DECam photometry, namely the diffusive effects of lateral electric field variations in the detectors. In the next section, we will make the case that the patterns observed in the PS1 photometry residuals are *not* caused by this mechanism, but are instead caused by variations in the *vertical* electric field (the field direction perpendicular to the CCD surface).

First, in this section, we will describe how we have measured the presence or absence of these tree-ring patterns in 5 types of data. For all of these examples, we use a single GPC1 CCD (XY40) to illustrate the effects in detail, but a similar set of effects are seen in many, if not all, of the GPC1 detectors with varying strengths. First, we show the residual PSF photometry. Second, we show the residual aperture photometry. Third, we show the astrometric residual patterns. Fourth, we show the patterns observed in the flat-field images. Finally, we show measurements derived from the second-moments of the stars.

For all effects discussed below, we are measuring the mean value of the effect in 10x10 pixel superpixels across the detector. The resulting images are all constructed so that a given superpixel represents the same range of true GPC1 XY40 pixels regardless of the type of measurement. To generate the photometry, astrometry, or second-moment plots, measurements were extracted from the PV0 DVO database (Magnier et al. 2016a) for observations covering the region $(\alpha, \delta) = (90° – 150°, -25° – 10°)$. This region of the sky provides a fairly high density of stars, but avoids the Galactic Plane where confusion may potentially contaminate the measurement. We limit the analysis to good measurements (PSF_QF $> 0.85$, see Magnier et al. 2016b) of likely stars ($|m_{psf} - m_{aper}| < 0.2$). Only measurements with instrumental magnitude $< -8.0$ ($-2.5 \log \mathrm{cts\ sec^{-1}} < -8.0$) are included to ensure reasonable signal-to-noise per measurement. We require at least 2 measurements in a given filter and at least 5 measurements total for any star included in the analysis.

### 3.1. Photometric Residuals

Figure 1 shows the 2D patterns of PSF photometry residuals. In this case, we select PSF magnitude measurements for detections of stars which fall in the given superpixel. We subtract each measurement from the average magnitude for the object in the selected filter ($\delta m_{psf} = \overline{m}_{psf} - m_{psf}$) to determine the residual magnitude, excluding as an outlier any measurement with $|\delta m_{psf}| > 0.5$. For a given superpixel, we measure

Table 1: Systematic Trends : Standard deviation by filter

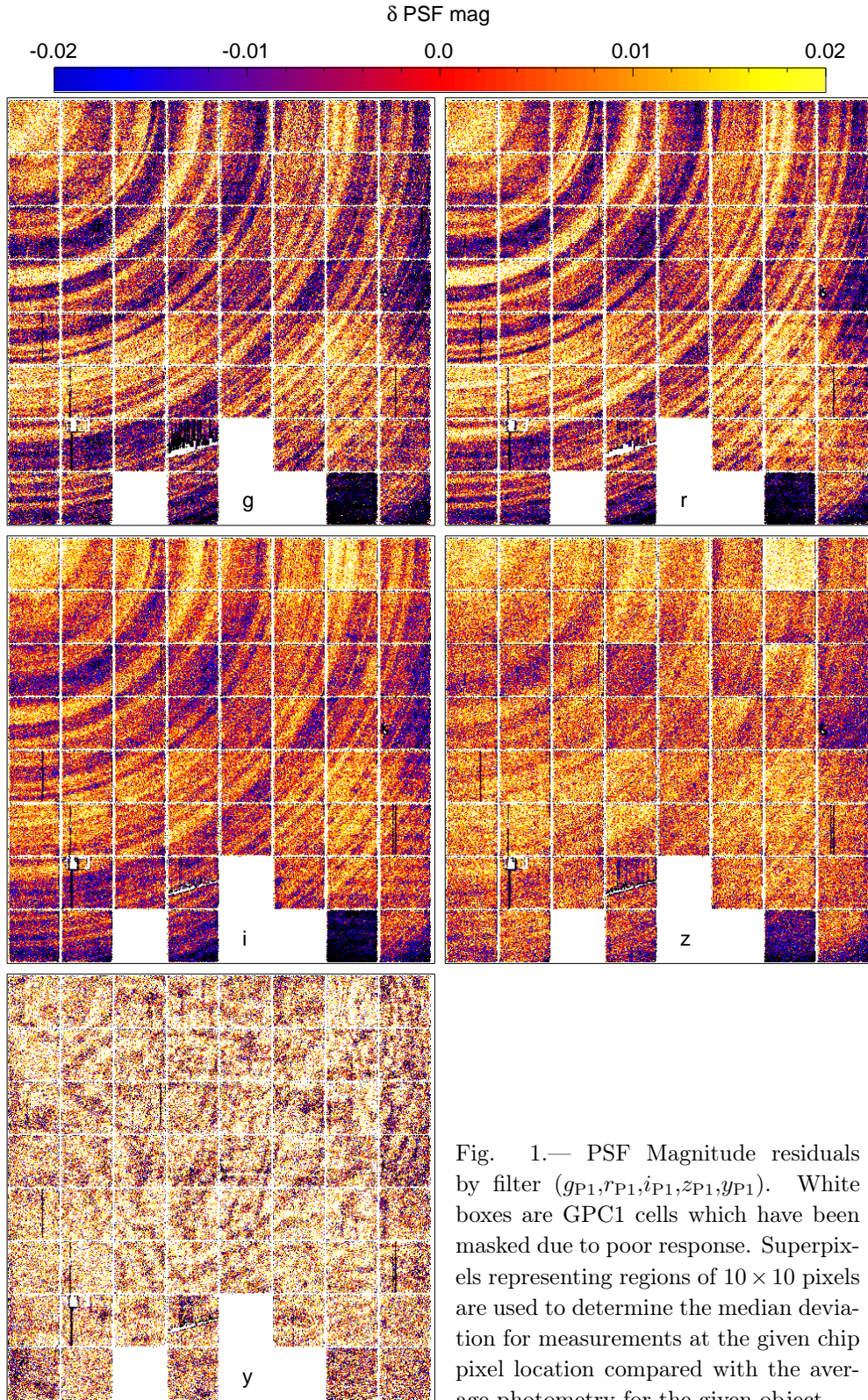| Filter | psf mags | ap mags | astrom | smear | flat |
|--------|----------|---------|--------|-------------------|-------|
|        | mmags    | mmags   | mas    | pixels$^2$ | mmags |
| $g_{\mathrm{P1}}$ | 11.8 | 13 | 8.0 | 0.169 | 3.0 |
| $r_{\mathrm{P1}}$ | 10.9 | 12 | 6.7 | 0.133 | 2.2 |
| $i_{\mathrm{P1}}$ | 8.5 | 10 | 6.0 | 0.069 | 1.7 |
| $z_{\mathrm{P1}}$ | 8.7 | 12 | 5.5 | 0.052 | 3.2 |
| $y_{\mathrm{P1}}$ | 16.5 | 26 | 6.8 | 0.059 | 15.3 |

Fig. 1.— PSF Magnitude residuals by filter ($g_{P1}$,$r_{P1}$,$i_{P1}$,$z_{P1}$,$y_{P1}$). White boxes are GPC1 cells which have been masked due to poor response. Superpixels representing regions of $10 \times 10$ pixels are used to determine the median deviation for measurements at the given chip pixel location compared with the average photometry for the given object.
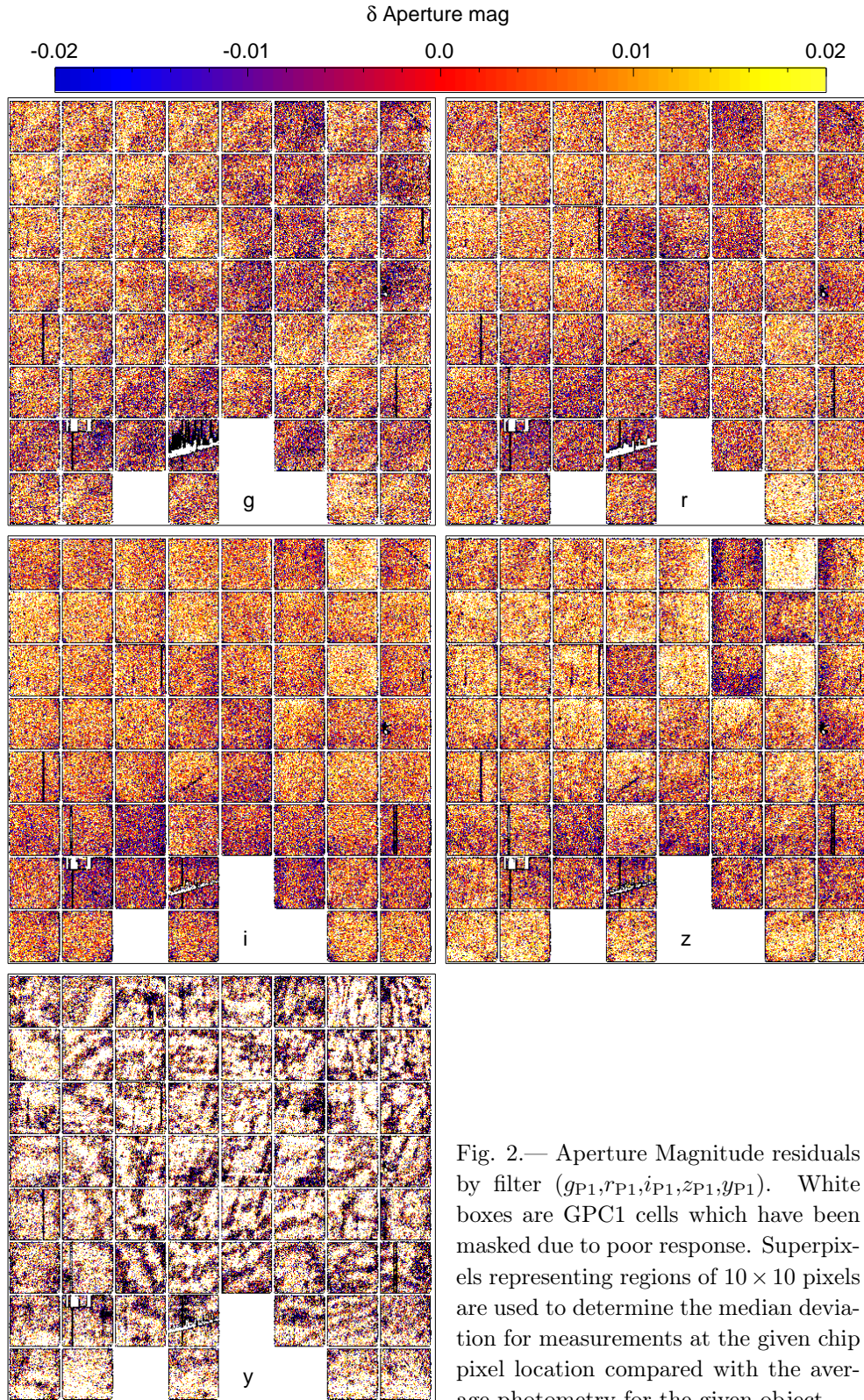
Fig. 2.— Aperture Magnitude residuals by filter ($g_{P1}$,$r_{P1}$,$i_{P1}$,$z_{P1}$,$y_{P1}$). White boxes are GPC1 cells which have been masked due to poor response. Superpixels representing regions of $10 \times 10$ pixels are used to determine the median deviation for measurements at the given chip pixel location compared with the average photometry for the given object.

the median of the $\delta m_{psf}$ distribution. The figure shows $\delta m_{psf}$ for each filter ($g_{\rm P1}$,$r_{\rm P1}$,$i_{\rm P1}$,$z_{\rm P1}$,$y_{\rm P1}$). The dynamic range of the color scale is from -20 to +20 millimagnitudes for all 5 plots.

The tree-ring pattern is clearly visible for the four blue filters, but finging dominates the pattern for $y_{\rm P1}$. Small offsets of individual cells are also apparent for $z_{\rm P1}$. While the patterns are clear across the image, the signal-to-noise of the structures per pixel is not very strong in these images. The per-pixel standard deviations of these plots are listed in Table 1. The per-pixel standard deviation is comparable to the amplitude of the correlated structures, so we need to integrate along the radial structures to make stronger statements about these patterns.

Figure 2 shows the equivalent measurement for aperture photometry instead of PSF photometry. The finging pattern again dominates the plot for $y_{\rm P1}$, but the tree rings are not seen in any of the filters. A diagonal pattern is visible in $g_{\rm P1}$ which is not observed in the PSF magnitudes. While the per-pixel scatter is somewhat (10% to 20%) higher for these aperture magnitudes than for the PSF magnitudes (Table 1), a structure with the amplitude of the PSF magnitude tree-rings would certainly have been obvious.

## 3.2. Astrometric Residuals

Figure 3 shows a similar type of measurement for astrometric residuals. To generate this plot, we use the same selection of measurements for astrometry as for photometry. In this case, we extract the residual in both the RA and DEC directions ($\delta RA = \overline{RA} - RA_i$, $\delta DEC = \overline{DEC} - DEC_i$) and rotate these values to the chip coordinate system ($\delta X, \delta Y$) using our knowledge of the chip orientation on the sky. We again exclude as bad any measurement with $|\delta X|$ or $|\delta Y| > 0.5$ arcsec before measuring the median values for each superpixel. We have determined the approximate center of the circular tree-ring pattern as (-5,4960) for this particular chip based on the pattern of the X astrometry displacements. Using this coordinate as the center of the pattern, we have converted the $\delta X, \delta Y$ offsets into $\delta R, \delta\theta$ measurements ($\delta R$ : radial component away from the center of the pattern, $\delta\theta$ : tangential component).

Figure 3 shows the 2D patterns of $\delta R$ for each filter ($g_{\rm P1}$,$r_{\rm P1}$,$i_{\rm P1}$,$z_{\rm P1}$,$y_{\rm P1}$). The dynamic range of the color scale is from -20 to +20 milliarcseconds for all 5 plots. A tree-ring pattern is visible for all five filters, with systematic structures following a circular pattern centered on the chip corner; the finging pattern is not apparent in the $y_{\rm P1}$ astrometry. The per-pixel standard deviations of these plots are listed in Table 1. The signal-to-noise of these structures is again somewhat weak, but the pattern is clearly visible in these figures.

## 3.3. Flat-field Structures

Figure 4 shows the high-spatial-frequency structures in the flat-field images. For this measurement, we have used a set of monochromatic flat-field images obtained with a tunable laser. The laser is used to illuminate our flat-field screen which is then observed by the PS1 telescope. These flat-field images were obtained 2011 Feb 09 as part of a campaign to study the PS1 system response (Tonry et al. 2012). Flats were obtain in a set of 4nm steps sampling the spectral response curve of each filter. To enhance the signal-to-noise, we have median-combined a set of 6 flats at the wavelength center of the corresponding filter.

In order to mask pixels which do not flatten well, we generate a copy of the image smoothed with a Gaussian kernel with $\sigma = 1.5$ pixels. Any pixels in the smoothed image which deviate from the median value in the image by more than 4 standard deviations are masked. We generate the superpixel image by
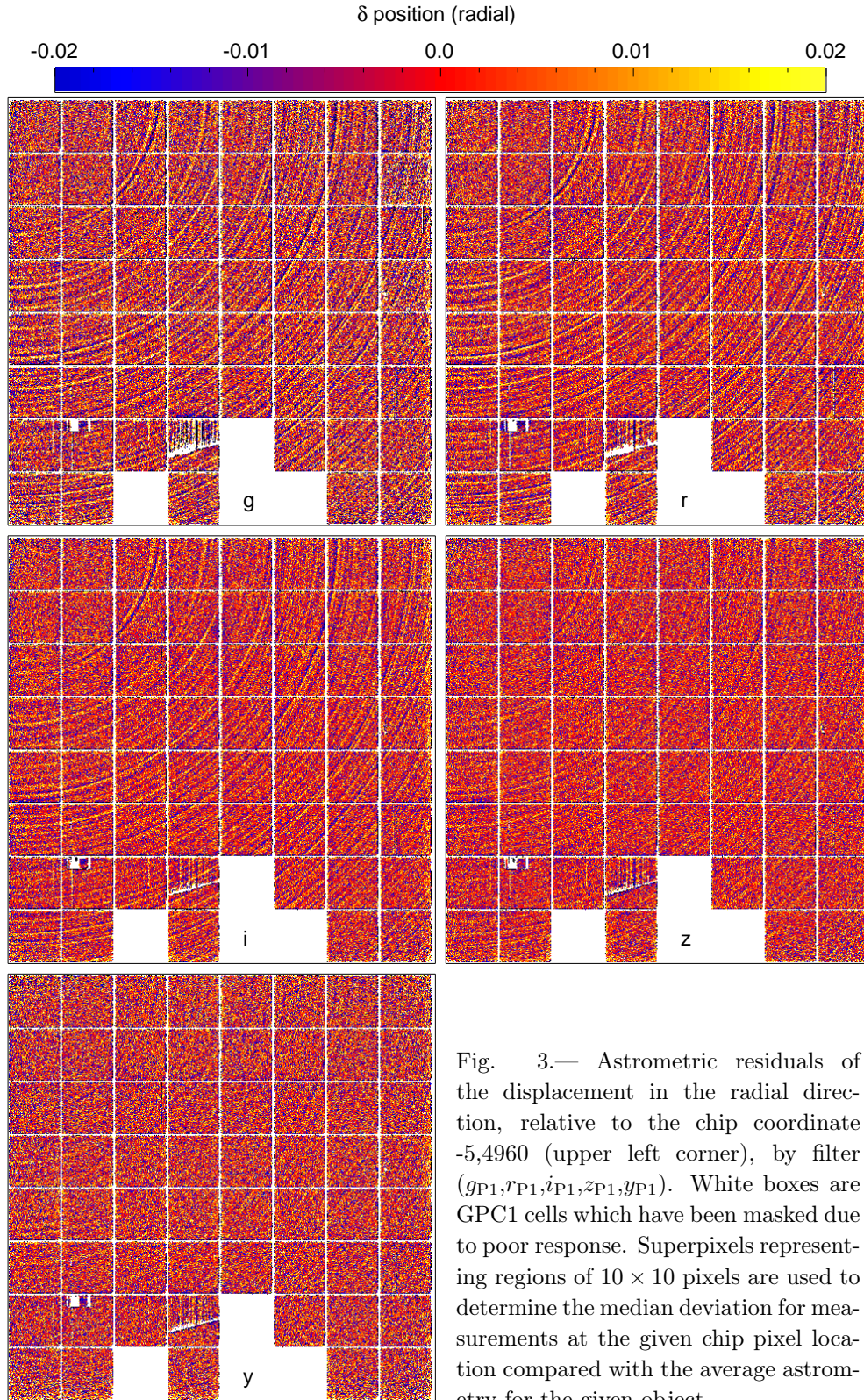
Fig. 3.— Astrometric residuals of the displacement in the radial direction, relative to the chip coordinate -5,4960 (upper left corner), by filter ($g_{P1}$, $r_{P1}$, $i_{P1}$, $z_{P1}$, $y_{P1}$). White boxes are GPC1 cells which have been masked due to poor response. Superpixels representing regions of $10 \times 10$ pixels are used to determine the median deviation for measurements at the given chip pixel location compared with the average astrometry for the given object.
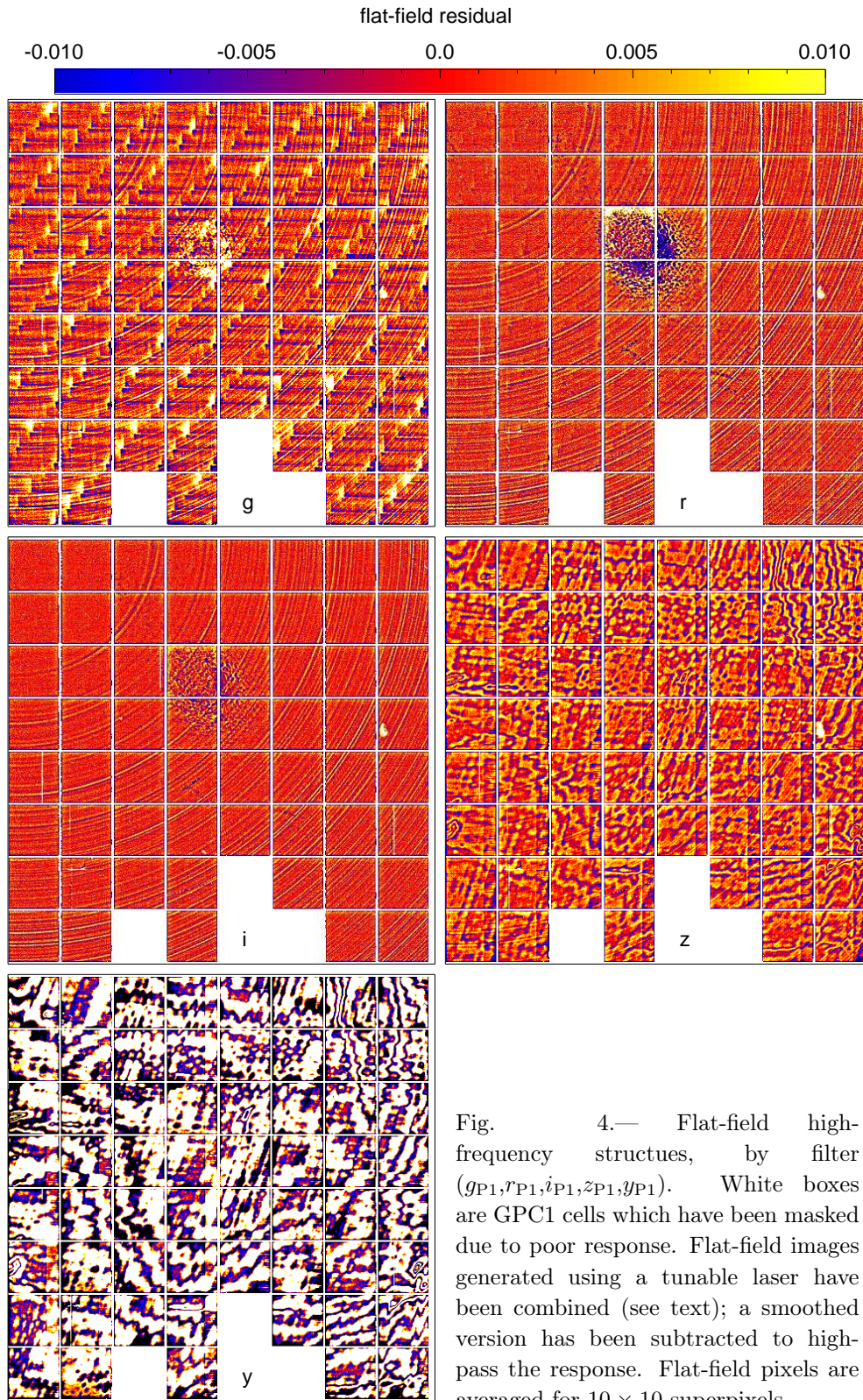
flat-field residual



Fig. 4.— Flat-field high-frequency structues, by filter $(g_{P1}, r_{P1}, i_{P1}, z_{P1}, y_{P1})$. White boxes are GPC1 cells which have been masked due to poor response. Flat-field images generated using a tunable laser have been combined (see text); a smoothed version has been subtracted to high-pass the response. Flat-field pixels are averaged for $10 \times 10$ superpixels.

averaging the unmasked pixels associated with each superpixel.

Figure 4 shows the superpixel images for the flat-fields in the five filters. These flat-field images are displayed as fractional deviations relative to the median flat-field image and can thus be compared to the magnitude residuals. When flattening an image, these flat-fields would be divided into the flux of the raw image. The residuals are thus defined in the sense that a positive feature in these flats which does *not* represent a real quantum efficiency deviation would induce a *reduction* in the measured flux in those pixels, and thus a *negative* deviation in $\delta m_{psf}$ as defined above. The dynamic range of the color scale in these plots is -0.01 to +0.01. The tree-ring pattern is strong in the $(g_{P1}, r_{P1}, i_{P1})$ images, but nearly swamped by fringing in $z_{P1}$, and completely lost to finging in $y_{P1}$. A diagonal banding pattern is also seen in $g_{P1}$: this feature is thought to be due to the lithography process used to generate the CCD. A blob can also been seen covering 4 cells near the center of this chip; this is apparently a deposit of some kind on the detector. Both of the latter two effects behave like quantum efficiency variations and are removed well by standard flat-field techniques. Note that a small amount of the diagonal banding pattern remains in the aperture magnitude residuals for $g_{P1}$. For the rest of this article, we ignore these features and concentrate on the tree-ring features.

In order to suppress the large-scale structures for a quantitative analysis of the tree rings, we high-pass filter the superpixel image by subtracting a copy smoothed with a Gaussian of $\sigma = 3.0$ superpixels.

### 3.4. Second Moments

During the image analysis, the second moments are measured for all stars. The values can be used to assess changes in the shape of stars on the image. To measure changes in the shapes, we have extracted the second moments for all stellar detections, subject to the same selections as for the photometry and astrometry residuals (good stars, multiple detections). The second moments are measured with a Gaussian weighting function, with the $\sigma_w$ scaled by the PSF size so that the $\sigma$ measured for PSF stars is $\sim 65\%$ of $\sigma_w$. (Note that, since the measured $\sigma$ of stellar objects is biased down by the weighting function, this is not quite the same as having $\sigma_w = 1.6$ times the true PSF $\sigma$; see discussion in Magnier et al. 2016b). For each stellar detection, we extract the values $M_{xx,xy,yy} = \sum F_i w_i (x^2, xy, y^2) / \sum F_i w_i$. For each exposure, we find the median second moments for PSF objects on this chip (XY40) and subtract those median values from the instantaneous measurements of $M_{xx,xy,yy}$. We then determine the median of the residual second moments for each superpixel, resulting in 3 images ($\delta M_{xx,xy,yy}$) for each filter.

Using the second moment images, we can construct certain interesting combinations, inspired by discussions of lensing measurements (Kaiser et al. 1995):

$$e_0 = \delta M_{xx} + \delta M_{yy} \tag{1}$$

$$e_1 = \delta M_{xx} - \delta M_{yy} \tag{2}$$

$$e_2 = \sqrt{e_1^2 + 4\delta M_{xy}} \tag{3}$$

For a 2D Gaussian profile with an elliptical contour, these values are related to the shape of the elliptical contour as follows:

$$e_0 = \sigma_{\text{major}}^2 + \sigma_{\text{minor}}^2 \tag{4}$$

$$e_1 = (\sigma_{\text{major}}^2 - \sigma_{\text{minor}}^2) \cos(2\theta) \tag{5}$$

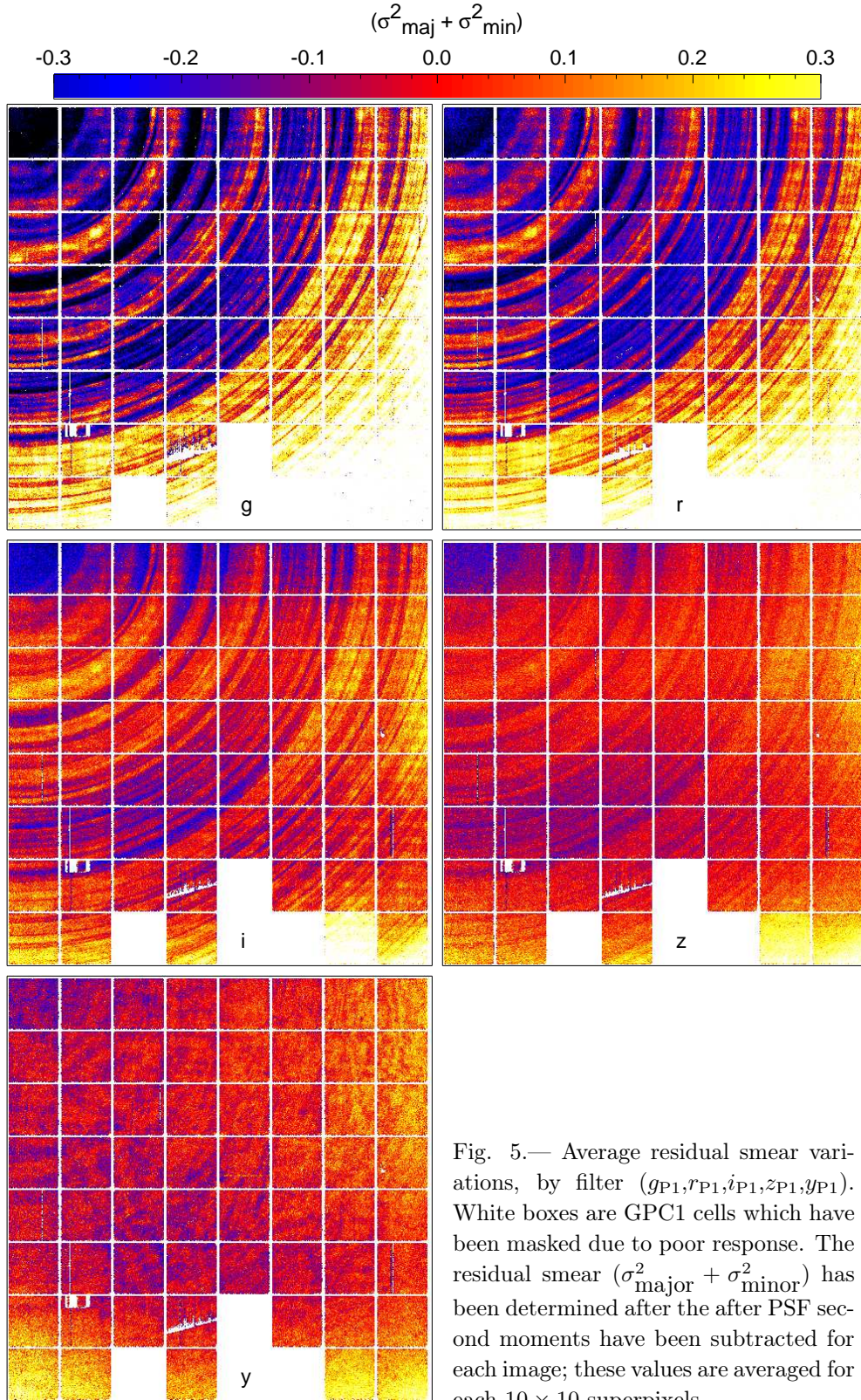$$e_2 = \sigma_{\text{major}}^2 - \sigma_{\text{minor}}^2 \tag{6}$$

Fig. 5.— Average residual smear variations, by filter ($g_{P1}$,$r_{P1}$,$i_{P1}$,$z_{P1}$,$y_{P1}$). White boxes are GPC1 cells which have been masked due to poor response. The residual smear ($\sigma^2_{\mathrm{major}} + \sigma^2_{\mathrm{minor}}$) has been determined after the after PSF second moments have been subtracted for each image; these values are averaged for each $10 \times 10$ superpixels.
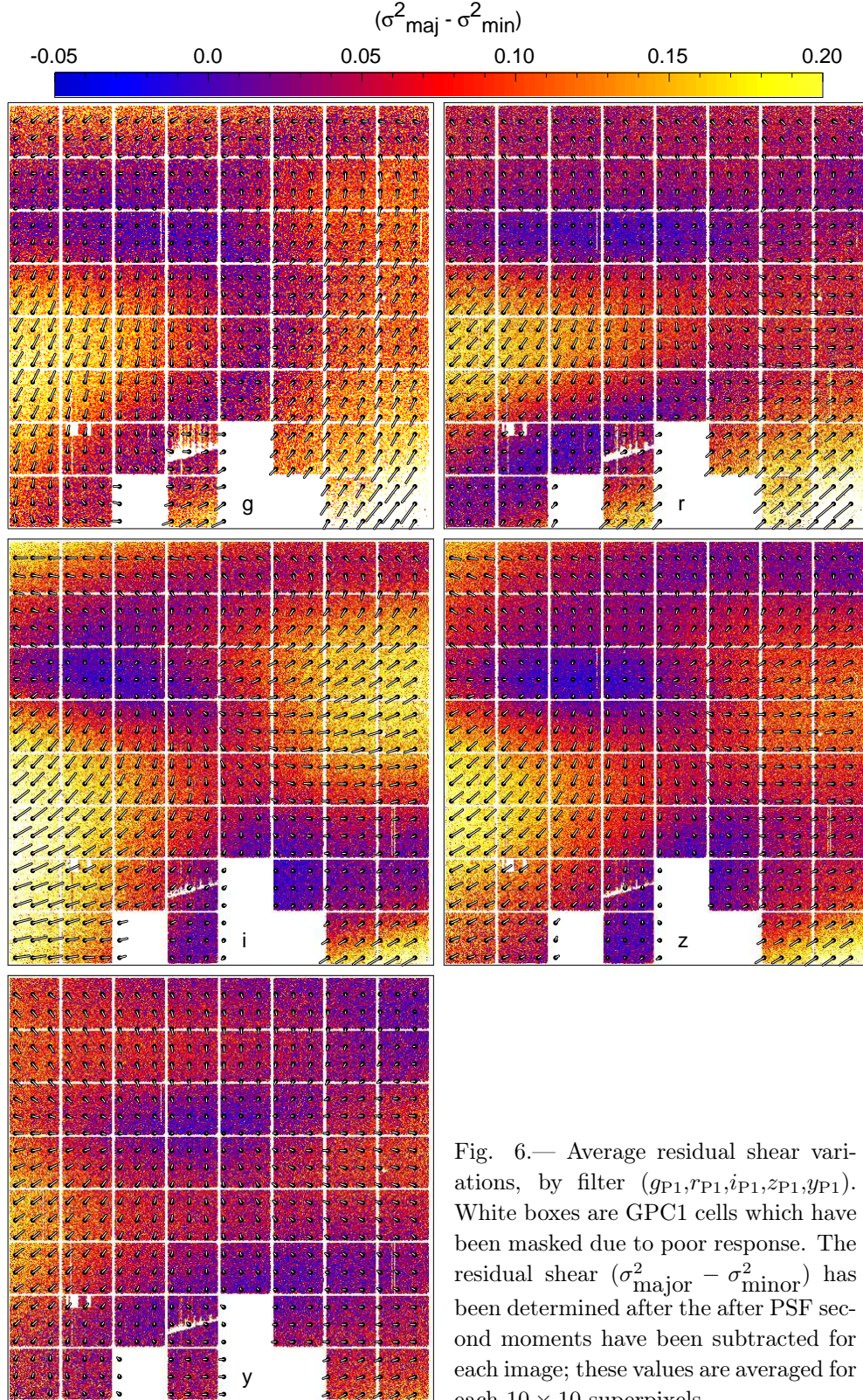
Fig. 6.— Average residual shear variations, by filter $(g_{P1}, r_{P1}, i_{P1}, z_{P1}, y_{P1})$. White boxes are GPC1 cells which have been masked due to poor response. The residual shear $(\sigma^2_{\mathrm{major}} - \sigma^2_{\mathrm{minor}})$ has been determined after the after PSF second moments have been subtracted for each image; these values are averaged for each $10 \times 10$ superpixels.

Where $\sigma_{\mathrm{major}}$ and $\sigma_{\mathrm{minor}}$ are the major and minor axis dimensions of the ellipse and $\theta$ is the position angle. Thus, $e_0$ is a measurement of the change in the size of the stellar PSFs as a function of position in the detector ("smear"), $e_2$ is a measurement of the change in ellipticity of the stellar PSFs ("shear"), and we can determine the angle of the PSF ellipticity from the $e_1$ term.

Figure 5 shows the spatial trend of the smear, $e_0$. The dynamic range of these images is -0.3 to +0.3 pixel$^2$. A tree-ring pattern is visible for all 5 filters, though $y_{\mathrm{P1}}$ is dominated by the fringing pattern. Structures with relatively low spatial frequencies can also be seen.

Figure 6 shows the spatial trend of the shear, $e_2$. This value is positive definite and is plotted with a color scale ranging from -0.02 to 0.22 pixel$^2$. Overlayed on Figure 6 is a set of vectors representing the ellipse orientation as a function of postion. The length of the vectors corresponds to the value of $e_2$. The tree-ring structure is *not* apparent in this figure for any filter. The spatial variations are low-frequency and unrelated to the radial trend from the upper-left corner.

### 3.5. Correlations Between Tree-Ring Patterns

Tree-ring patterns are clearly seen in 4 of the measurement types above: the PSF photometry, the astrometry, the flat-field, and the smear terms. As discussed above, the signal-to-noise per pixel in the plots of the systematic trends is relatively low ($\sim$1.0). While the tree-ring patterns are apparent in many of these figures, there are also some other systematic structures which may degrade the signal further.

To quantitatively compare the tree-ring trends between filters and between the types of measurements, we need to measure the tree-ring structure explicitly and filter out the other effects if possible. To do this, we have applied a high-pass filter to all of the relevant images (PSF photometry residuals, astrometric residuals in the radial direction, flat-field residuals, and second moment smear terms) to remove unrelated spatial structures. We have then measured the median of the signal in radial bins centered on (-5,4960) across an arc from $\phi$ = -20° to -50°(as measured relative to the top row of the images). We have selected a small fraction of the arc to minimize the error associated with the choice of the pattern center and to avoid several bad cells near the bottom of the chip.

For a given type of measurement, the systematic effect is strongly correlated between filters. The strongest correlation is the smear term: Figure 8 shows the correlation of the smear pattern between $g_{\mathrm{P1}}$ and the other four filters. Even $y_{\mathrm{P1}}$ is strongly correlated with $g_{\mathrm{P1}}$ despite the presence of the fringe pattern. PSF photometric residuals are also correlated between filters, as shown in Figure 9. Here, the $y_{\mathrm{P1}}$ correlation with $g_{\mathrm{P1}}$ is quite weak: the fringing pattern dominates the tree rings for PSF photometry. The radial component of the astrometric residual is also well correlated between filters, with no loss of correlation due to fringing

Table 2: Systematic Trends : Correlations by filter

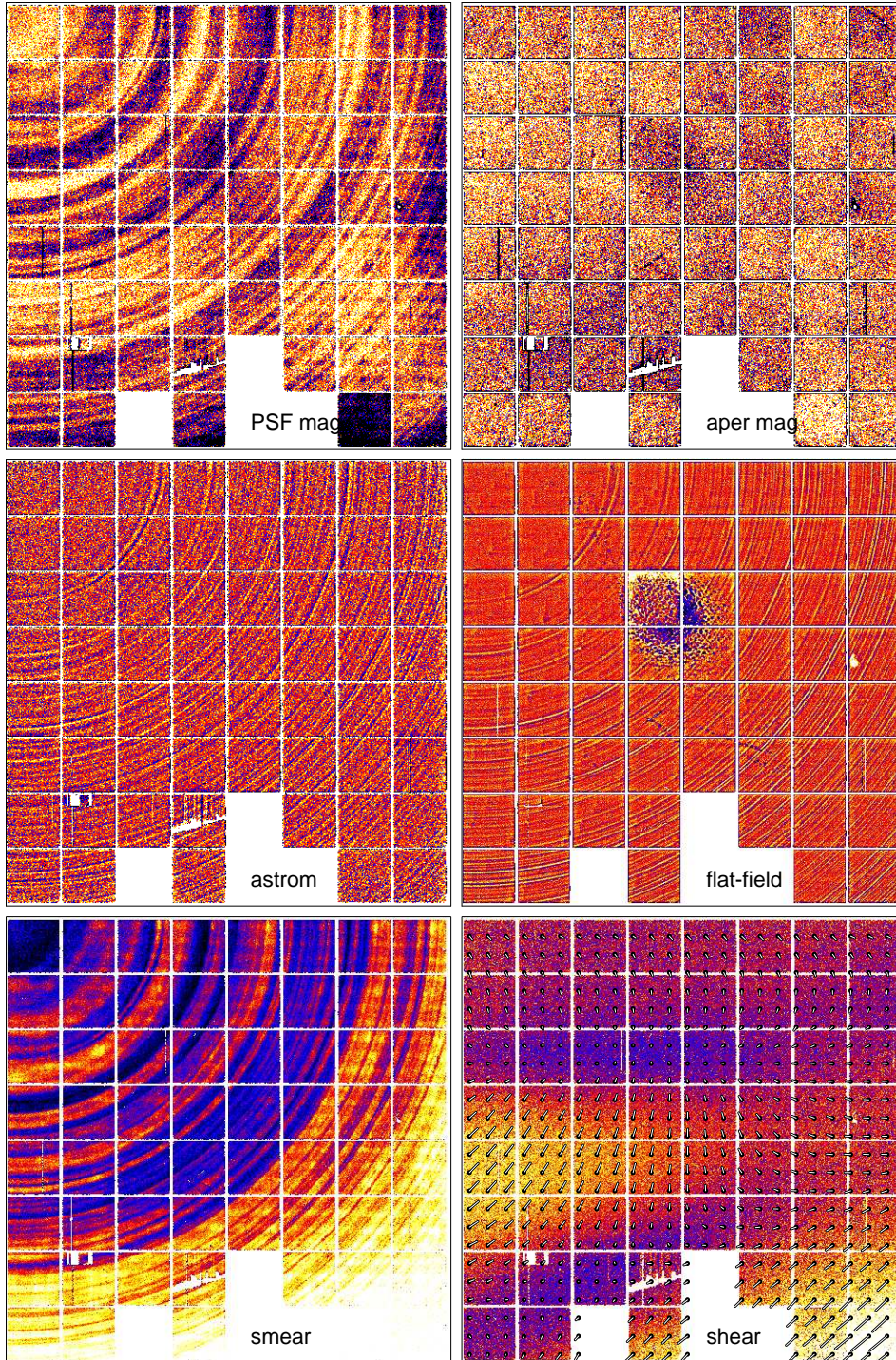| Filter | smear | psf mags | astrom | flat |
|---|---|---|---|---|
| $g_{\mathrm{P1}}$ | 1.00 | 1.00 | 1.00 | 1.00 |
| $r_{\mathrm{P1}}$ | 0.78 | 0.84 | 0.84 | 0.76 |
| $i_{\mathrm{P1}}$ | 0.40 | 0.50 | 0.66 | 0.64 |
| $z_{\mathrm{P1}}$ | 0.16 | 0.26 | 0.37 | 0.33 |
| $y_{\mathrm{P1}}$ | 0.10 | 0.10 | 0.25 | 0.30 |

Fig. 7.— All 6 measured effects for $r_{\mathrm{P1}}$. This figure illustrates the different spatial structure observed for each of the 6 patterns measured in this work. The PSF magnitude (upper-left) and smear residuals (lower-left) have a very clear common tree-ring structure, while the astrometric residual (middle-left) and flat-field residuals (middle-right) have their own common tree-ring pattern with much higher frequencies than the previous two effects. Aperture magnitude (upper-right) and shear residuals (lower-right) do not show a strong signal consistent with either of the two patterns.

in $y_{\rm P1}$. Finally, the flat-field residuals are generally correlated between filters, but both $z_{\rm P1}$ and $y_{\rm P1}$ are affected by fringing. For $y_{\rm P1}$, the correlation is completely washed out by the very strong fringing pattern.

For all four types of measurements, the slope of the fitted lines are listed in Table 2. There is a consistency in the trend from $g_{\rm P1}$, with the strongest systematic tree-ring effects to $y_{\rm P1}$, with the weakest effects. Note that the second moment smear and astrometry terms have different relative strength in $y_{\rm P1}$ compared with $g_{\rm P1}$.
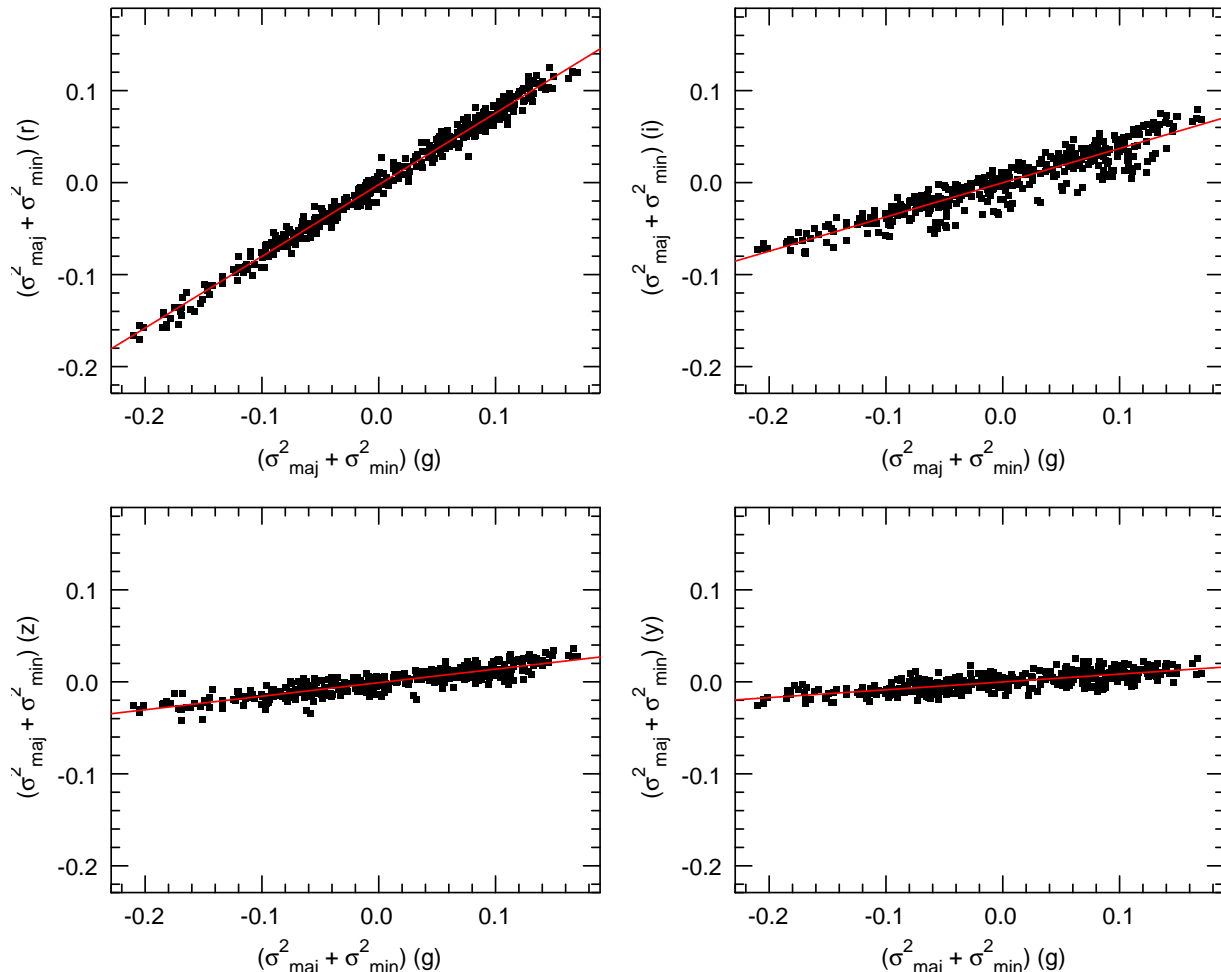


Fig. 8.— Correlation of the smear $(\sigma^2_{\rm major} + \sigma^2_{\rm minor})$ signal in $g_{\rm P1}$ with the other 4 bands: $r_{\rm P1}$ (upper-left), $i_{\rm P1}$ (upper-right), $z_{\rm P1}$ (lower-left), $y_{\rm P1}$ (lower-right).

An important question is the relationship of the tree-ring pattern between the different types of measurements. Different models for the tree-ring structures make different predictions about the correlations between different effects. Note the very different spatial structure between the different measurements in a given filter: the radial variations do not all follow the same patterns. Instead, we find the following relationships hold:
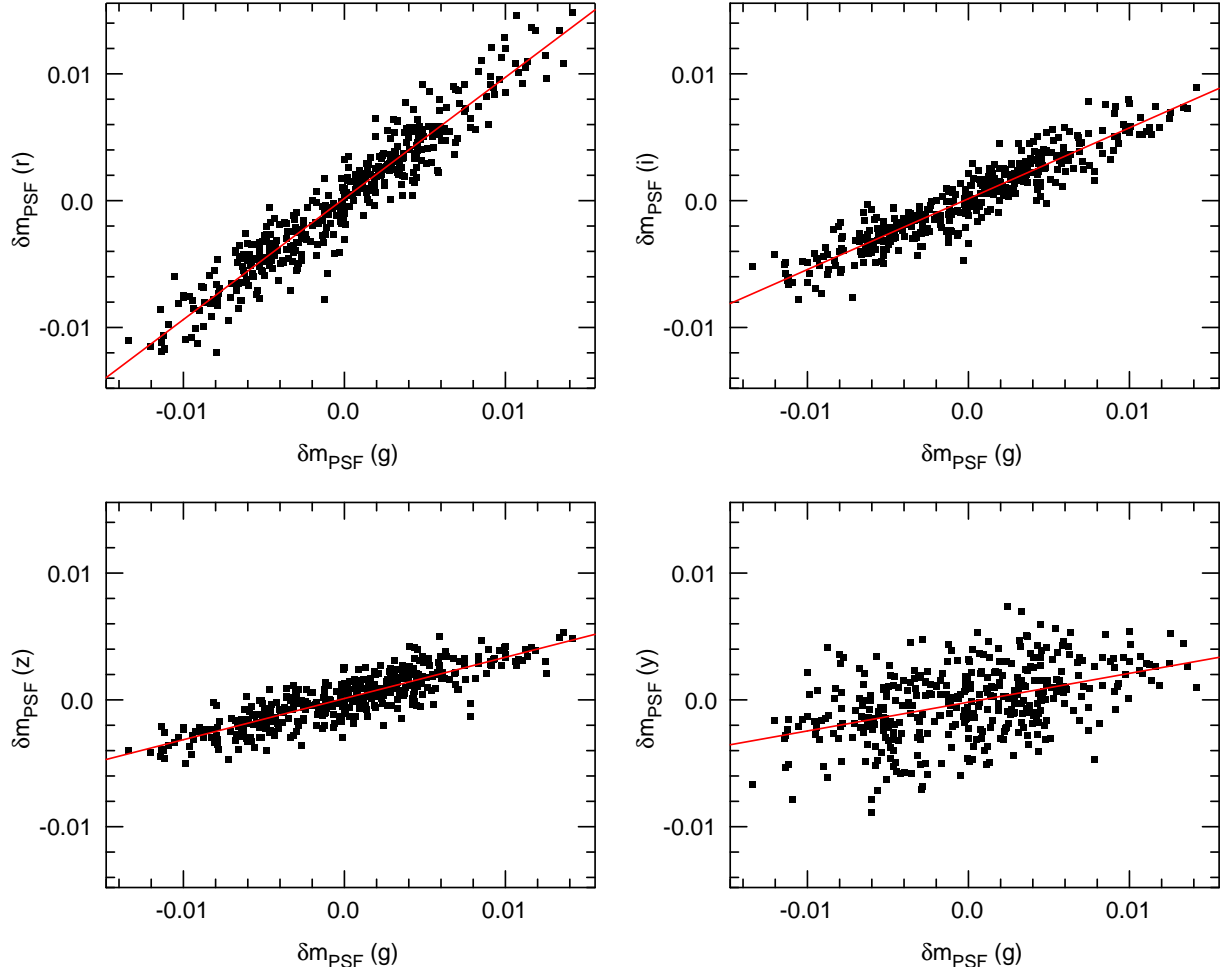
Fig. 9.— Correlation of the PSF magnitude residuals ($\delta m_{psf}$) in $g_{\mathrm{P1}}$ with the other 4 bands: $r_{\mathrm{P1}}$ (upper-left), $i_{\mathrm{P1}}$ (upper-right), $z_{\mathrm{P1}}$ (lower-left), $y_{\mathrm{P1}}$ (lower-right).
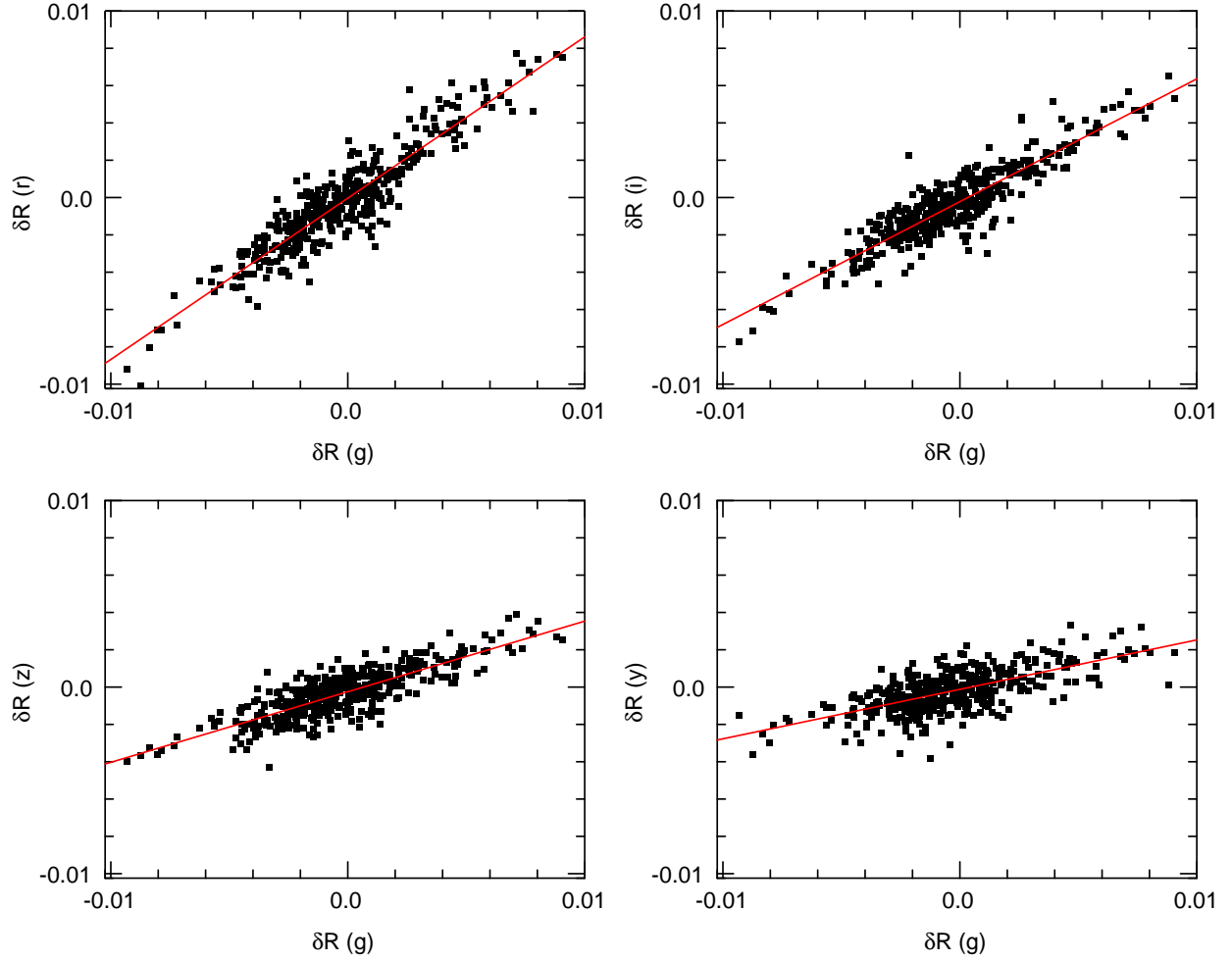
Fig. 10.— Correlation of the radial astrometric residual displacement ($\delta R$) in $g_{P1}$ with the other 4 bands: $r_{P1}$ (upper-left), $i_{P1}$ (upper-right), $z_{P1}$ (lower-left), $y_{P1}$ (lower-right).
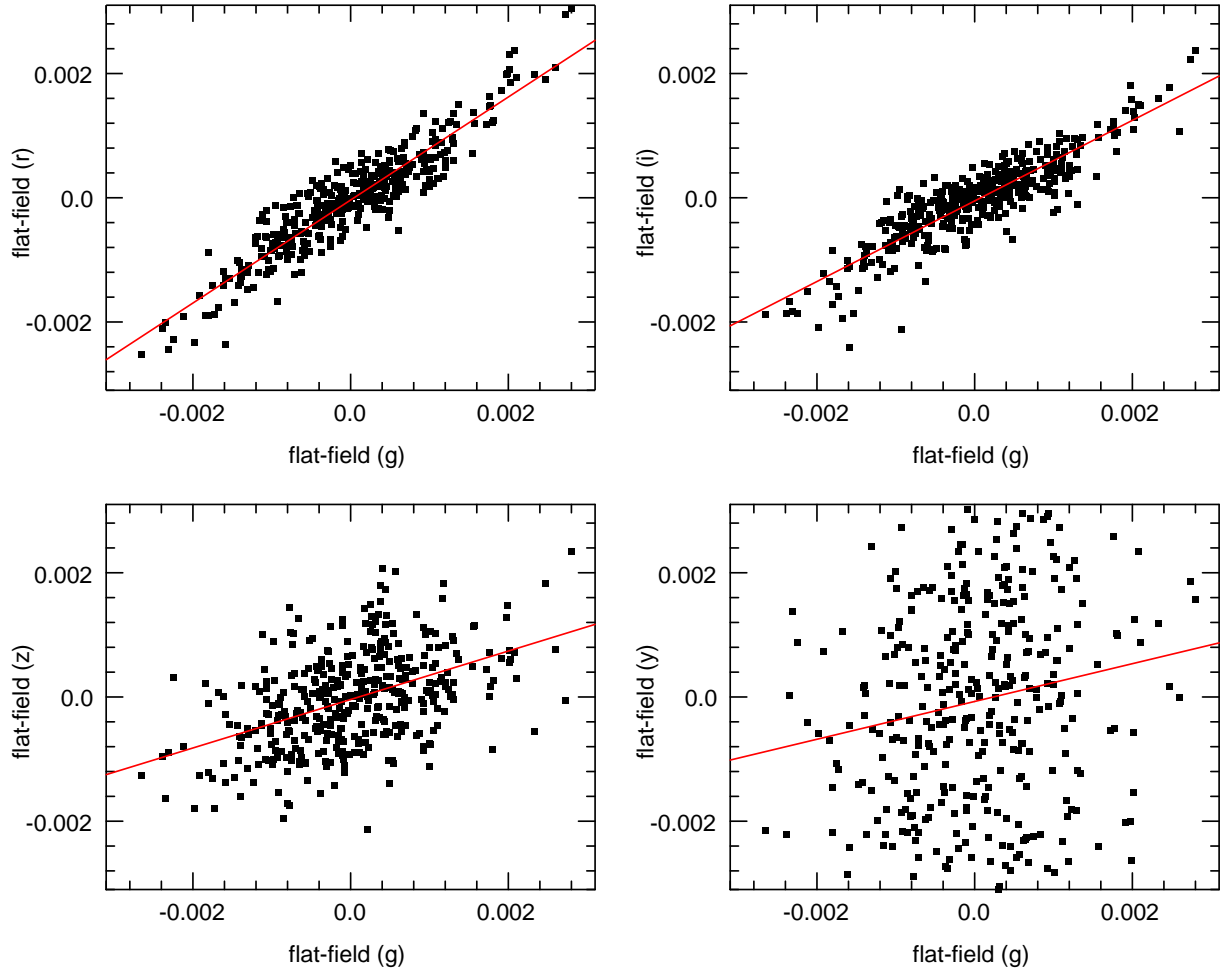
Fig. 11.— Correlation of the flat-field tree-ring structures in $g_{P1}$ with the other 4 bands: $r_{P1}$ (upper-left), $i_{P1}$ (upper-right), $z_{P1}$ (lower-left), $y_{P1}$ (lower-right).

First, the PSF magnitude residuals and the second-moment smear trends are strongly anti-correlated: regions which have larger PSFs than the mean tend to have smaller measured PSF fluxes than the mean (note that $\delta m_{psf}$ is defined so that positive values correspond to larger fluxes). These trends are shown in Figure 12.

Second, the radial derivative of the smear is anti-correlated with the radial component of the astrometric residuals: $\frac{\partial(\sigma^2_{major}+\sigma^2_{minor})}{\partial radius} \sim \delta R$ (see Figure 13).

Finally, the radial derivative of the radial component of the astrometric residual is anti-correlated with the flat-field residual errors: $\frac{\partial \delta R}{\partial radius} \sim \delta flat$ (see Figure 14). This last relationship is somewhat weakly measured. Because of the periodic nature of the tree rings, it is also difficult to be completely certain that the flat-field is proportional to the derivative of the astrometry residual, rather than the astrometry residual being proportional to the derivative of the flat-field. The correlation is somewhat weaker for derivative of the flat-field vs astrometry residual. The correlation is very weak between the flat-field and the astrometry residual values without a derivative. We are convinced that we have the sense of the derivative correct by examination of specific features in each image.

## 4.   Discussion

These trends measured above (Section 3) help to illuminate the underlying causes of these different effects.

First, if we consider the smear pattern (Figure 5), the measurement shows that the intrinsic sizes of the stellar images are varying in a radial sense between the different tree-ring regions. Although images experience an average image quality (due to seeing and focus) across the chip which may vary substantially from exposure to exposure, stars landing in the different tree-ring regions are consistently somewhat larger or somewhat smaller than that average.

Next, we can explain the correlation between the PSF photometry residuals and the observed smear (Figure 12). In the photometry analysis, we model the PSF allowing for some spatial variation in the shape. However, we have a limited number of stars to measure any spatial variation. Thus the 2D variations are sampled on a very coarse (e.g., $3 \times 3$) grid for each chip: the PSF parameters may vary smoothly across the chip following the bilinear interpolation between the $3 \times 3$ grid points. Thus, the spatial scale on which we model PSF variations is much larger than the spatial scale on which PSF variations are actually occuring, as illustrated by the changes in the smear plot (Figure 5). When the true PSF is larger than the model PSF, our model fits systematically underestimate the amount of flux in a given object. Conversely, when the true PSF is smaller, we overestimate the flux – this type of offset is a typical effect when mis-estimating the PSF

Table 3: Systematic Trends : Correlations between trends

| Filter | psf mags vs smear | $\nabla$ smear vs astrom | $\nabla$ astrom vs flat |
|---|---|---|---|
| $g_{P1}$ | -0.056 | -0.060 | -0.47 |
| $r_{P1}$ | -0.071 | -0.073 | -0.45 |
| $i_{P1}$ | -0.077 | -0.095 | -0.45 |
| $z_{P1}$ | -0.082 | -0.078 | -0.17 |
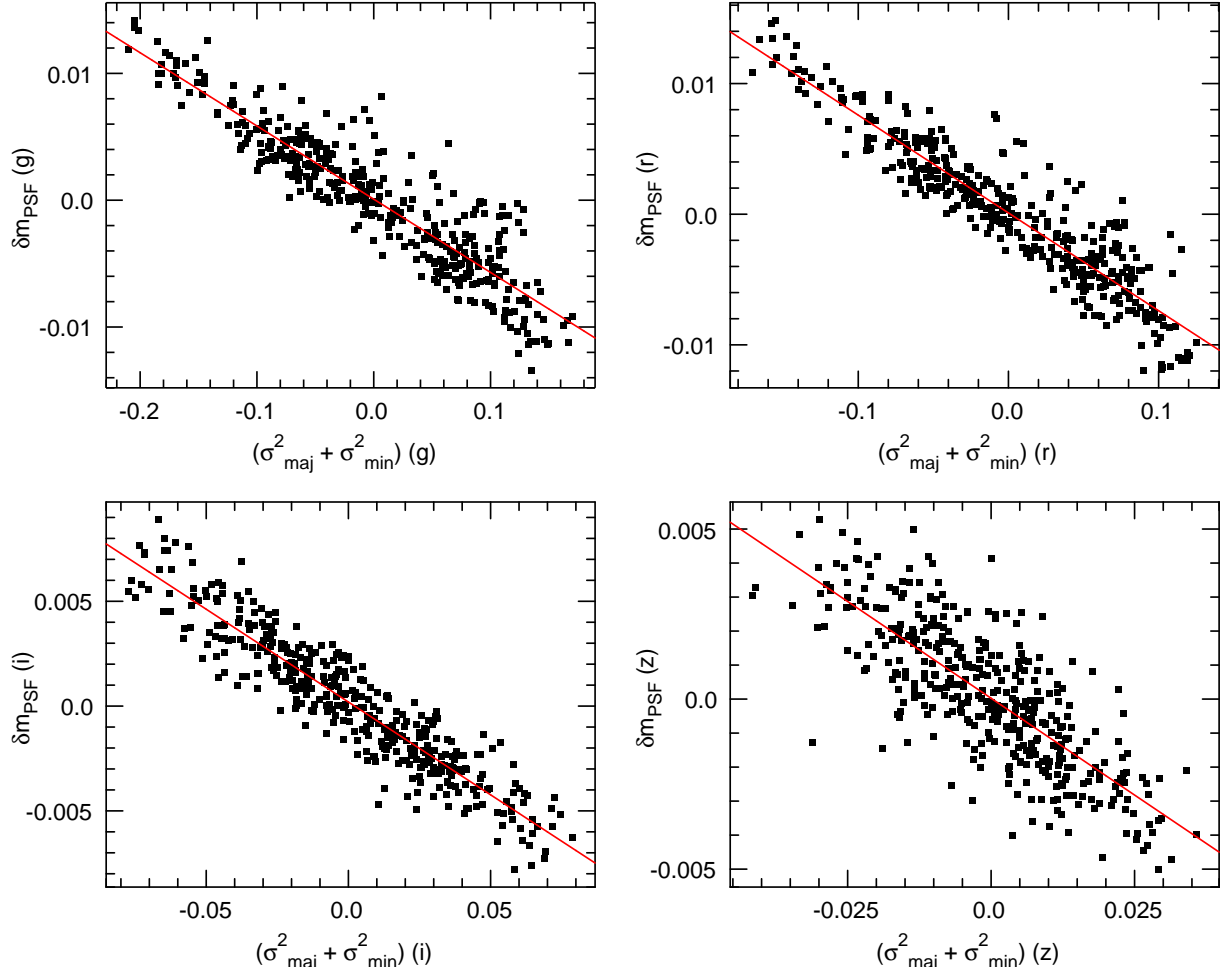
Fig. 12.— Correlation of the PSF magnitude residuals ($\delta m_{PSF}$) with the smear ($\sigma^2_{\mathrm{major}} + \sigma^2_{\mathrm{minor}}$) signal for $g_{\mathrm{P1}}$ (upper-left), $r_{\mathrm{P1}}$ (upper-right), $i_{\mathrm{P1}}$ (lower-left), $z_{\mathrm{P1}}$ (lower-right).
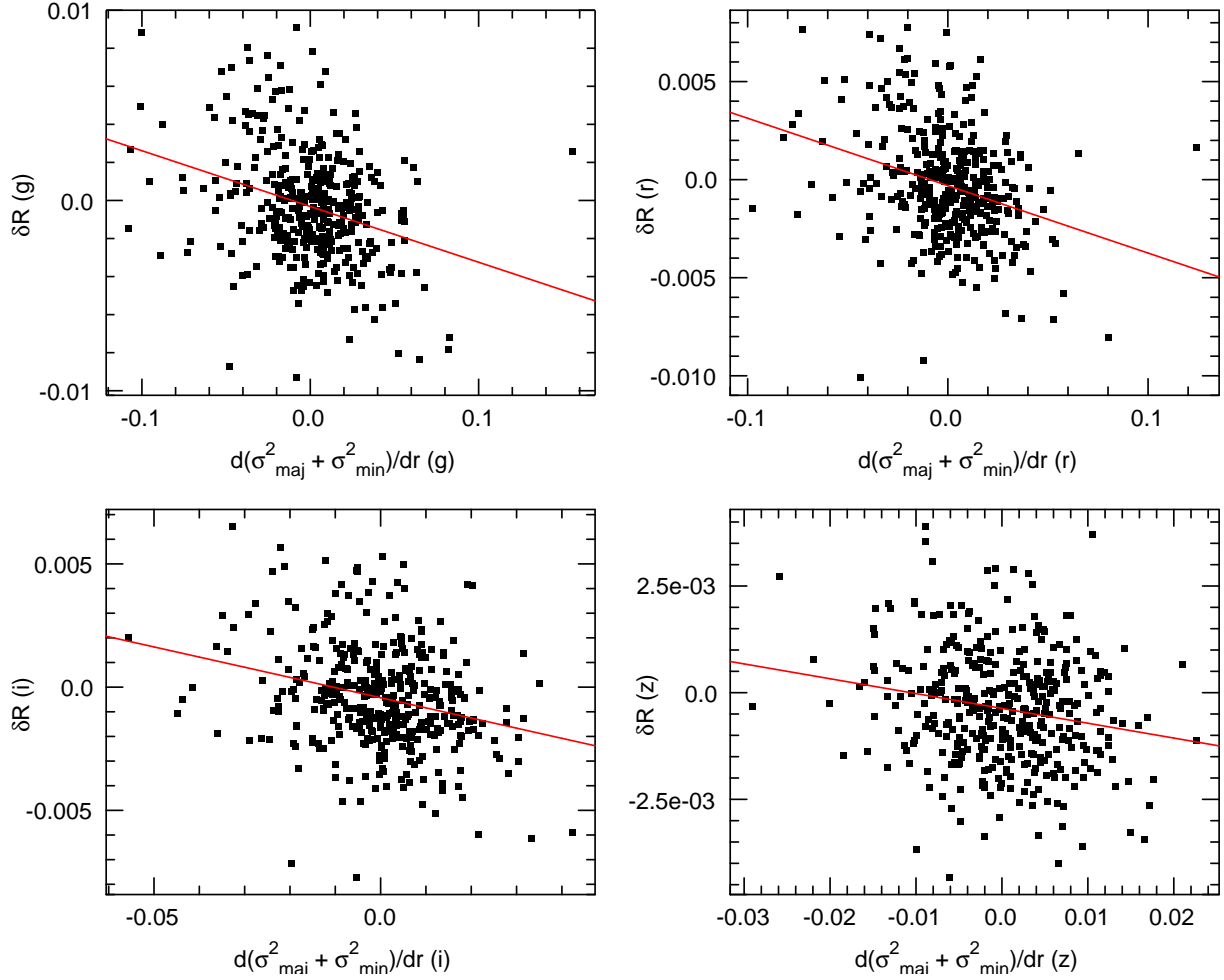
Fig. 13.— Correlation of the radial astrometric residual displacement ($\delta R$) with the derivative of the smear ($\partial \sigma^2_{\mathrm{major}} + \sigma^2_{\mathrm{minor}}$) signal with respect to the radial postion for $g_{\mathrm{P1}}$ (upper-left), $r_{\mathrm{P1}}$ (upper-right), $i_{\mathrm{P1}}$ (lower-left), $z_{\mathrm{P1}}$ (lower-right).
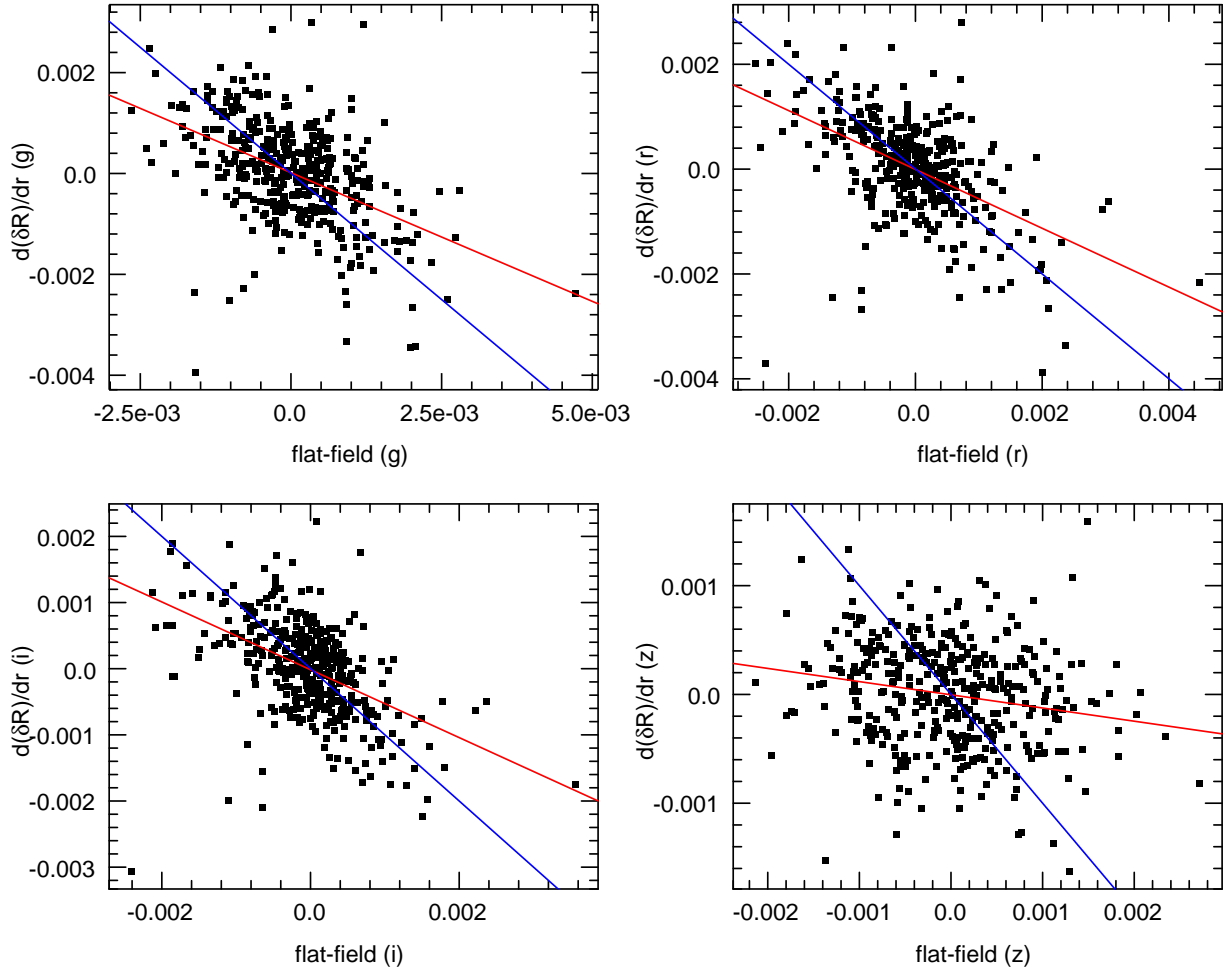
Fig. 14.— Correlation of the derivative of the radial astrometric residual displacement ($\delta R$) with respect to the radial position with the flat-field tree-ring signal for $g_{P1}$ (upper-left), $r_{P1}$ (upper-right), $i_{P1}$ (lower-left), $z_{P1}$ (lower-right).

size. The slope of the trend depends on the mean typical seeing for the given filter. For example, the $g_{P1}$ seeing is typically $1.3''$, corresponding to a Gaussian $\sigma$ of 2.15 pixels. A smearing of $\sigma_{major}^2 + \sigma_{minor}^2 = 0.1$ pixels$^2$ would increase the size by about 0.02 pixels, or 1%, roughly consistent with the observed photometric deviation of about 5 to 10 millimags for this amount of smearing.

The correlation between the flat-field structures and the radial derivative of the astrometric residual displacements in the radial direction (Figure 14) is consistent with radial variations in the plate-scale. The tree-rings observed by DES are completely attributed to effective plate scale changes. Effective plate scale changes result in flat-field deviations because the flat-field illumination is a source of constant surface brightness. Pixels see a varying amount of flux depending on their effective area. This changing plate scale also affects the astrometry since these variations occur on spatial scales much smaller than the astrometric model. In this description of the tree rings, the flat-field deviations are $-1 \times \frac{\partial \delta R}{\partial r}$. The best-fit slopes of our correlations are $\sim 0.5$, but the signal-to-noise is rather low. A slope of -1 appears to be consistent with our measurements.

The fact that the PSF ellipticity changes are *not* correlated with the tree-ring structure (Figure 6) tells us that, unlike the case for DES, the effective plate-scale changes seen in the flat-field and astrometry signals are not the dominant cause of the PSF photometry errors. Also, the fact that we do not measure significant aperture photometry errors correlated with the tree rings confirms this point. The amplitude of the flat-field errors are 1-2 millimagnitudes, much smaller than the PSF photometry errors, and far below the pixel-to-pixel noise in the aperture magnitude residuals. It is likely in our opinion that the plate-scale changes causing the flat-field and astrometry effects are affecting both the ellipticity and the aperture magnitudes, but the level of the effect is too small to see given the other systematic structures (in the shear plot) and the noise level (in the aperture magnitudes).

Finally, the correlation between the smear structures and the astrometry residuals shows that these two effects are connected. Although the correlation is weak in Figure 13, careful inspection of the location of these two tree ring patterns shows that the locations of the rings in the radial astrometric residual images occurs at the boundaries between regions with substantially different values of the smear signal.

We suggest that the underlying connection between all of these tree-ring effects is the pattern of the doping variations in the silicon. As discussed by Plazas et al. (2014), the tree-ring patterns seen by the DES team are caused by lateral electic fields in the detector silicon (in the plane of the CCD wafer) generated by variations in the space charges embedded in the silicon, in turn coming from low-level changes in the doping as the silicon boule is grown. We conclude that the astrometric and flat-field variations seen in our detectors are caused by these same types of doping variations. The changes in the smear (and thus the PSF magnitudes) are apparently also related to the doping variations. The lateral electric fields which introduce the astrometry and flat-field variations occur at the boundary between regions with higher and lower space charges from the dopant. Regions with high (or low) space charge density thus correspond to regions with relatively high (or low) amounts of smear; the astrometric deviations follow the gradient between these regions.

We interpret the changes in the smear term as changes in the amount of charge diffusion as the photoelectrons travel to the bottom of the pixel well. The blue filters exhibit the strongest changes in the amount of smear. These are also the filters for which the detected electrons have travelled the longest distance in the silicon, and are thus most affected by diffusion effects. Charge diffusion (as opposed to the charge drift caused by the lateral electric fields) results in a Gaussian smearing of the stellar profile: as the photoelectrons migrate from the site where they were generated by the incoming photon to the bottom of the pixel well,

they follow a random walk in the plane of the detector. The longer the electrons take to make the journey down to the bottom of the pixel, the further they are able to wander from their creation coordinate in the detector. Following the discussion in Holland et al. (2003), the amount of charge diffusion is thus related to the velocity of the electrons in the direction of the optical axis: $\sigma \sim \sqrt{2Dt}$ where $\sigma$ is the size of the smearing kernel, $t$ is the time required for the electrons to traverse the thickness of the silicon wafer, and $D$ is the diffusion coefficient. The velocity of the photoelectron, and thus the time to traverse the silicon, is related to the vertical electric fields in the silicon, which are caused by a combination of the applied voltages and the distribution of the space charges from the dopant. As shown by Holland et al. (2003), the charge diffusion is related to the space charge density by $\sigma \sim \rho^{-\frac{1}{2}}$ (their equation 6). Regions with high space charge densities increase the migration speed of the photoelectrons and reduce the amount of charge diffusion smearing; and vice versa for regions of low space-charge densities.

In summary, the variations in the space-charge density caused by variations in the dopant result in regions of higher and lower charge diffusion, and in turn regions with PSF photometry systematic residuals. The lateral gradients in the space-charge density induce lateral electric fields which in turn cause lateral motions of the photoelectrons, resulting in astrometric and flat-field deviations.

The DES team did not detect these charge diffusion variations. In that case, the amplitude of the photometric effects due to the lateral field are dominant; these include both the modification of the flat-field as well as PSF fitting errors due to the changing PSF sizes introduced by the varying effective pixels sizes. If the smearing effect reported here were as large for DES compared with the lateral PSF size changes as they are for GPC1, then the reported PSF photometry residuals for would have had very different characteristics. We conclude that, for DES, the lateral effects are much larger than the diffusion variations, compared with GPC1. The relative amplitude of these two effects depends on the details of the applied voltages, the amplitude of the space-charge density variations compared with the typical space-charge density, and the detector thicknesses. It is beyond the scope of this article to model these effects in detail.

## 5. Conclusion

The tree rings observed in the Pan-STARRS GPC1 data show two different effects, though they are related. First, the images are experiencing circularly-symmetric changes in the PSF size correlated with the tree-ring pattern. These PSF size changes drive errors in the PSF photometry on the scale of a few millimagnitudes, and are also correlated with the tree-ring pattern. These PSF size changes are consistent with changes in the charge diffusion, which also introduces a circularly symmetric smearing.

In addition, there are radial plate-scale changes correlated with the tree rings. These plate-scale changes introduce flat-field errors on the scale of ~1 millimagnitude and astrometric errors on the scale of 2-3 milliarcseconds. The observed relationship between the flat-field deviations and the radial derivative of the astrometric deviations confirms this interpretation (see also discussion in Plazas et al. 2014).

The spatial correlation of the gradient in the smear variations and the astrometric variations imply that both of these two types of tree ring effects are related, even though they manifest through different mechanisms. We conclude that the variations in both the vertical charge diffusion and the lateral charge migration are driven by changes in the electric field structures in the silicon due to the same variations in the doping structures in the silicon.

The small-scale variations in the charge diffusion observed in the Pan-STARRS detectors represents a

new type of systematic effect in deep depletion devices. This feature, if present in other detectors, could manifest in systematic errors in several ways. Like in the Pan-STARRS analysis example, the charge diffusion variations result in fine-structure in the observed stellar point-spread functions. For very precise photometry or morphological analysis, it will be necessary for the PSF models to account for the extra charge diffusion. Unlike the non-uniform pixel-size effects, correction of the PSF photometry cannot simply be performed as an average flat-field correction on the measurements after they have been processed. The additional smearing acts as a convolution with a Gaussian kernel of fixed size for a given filter. The photometry bias is a function of the fractional change of the PSF size. Thus, the introduced error depends on the average PSF for the image in question: an image with good image quality will suffer larger PSF model errors than an image with poor image quality. To account for this effect in a rigorous way, the analysis should use the measured diffusion variations to modify the model PSFs as a function of position before they are used for the image analysis.

The charge diffusion variations may also have an impact on spectroscopic measurements. Modern, precise spectroscopic measurements rely on precise measurements of the stellar line profiles. If such an analysis ignores variations in the charge diffusion, the measured line widths may be systematically biased.

This analysis points to the importance of careful instrumental characterization, especially for those instruments which are used for large-scale surveys with largely automatic data analysis systems and stringent precision goals.

## REFERENCES

Antilogus, P., Astier, P., Doherty, P., Guyonnet, A., & Regnault, N. 2014, Journal of Instrumentation, 9, C03048

Blouke, M. M., Janesick, J. R., Jall, J. E., & Cowens, M. W. 1981, in Proc. SPIE, Vol. 290, Society of Photo-Optical Instrumentation Engineers (SPIE) Conference Series, 6

Chambers, K. C., Magnier, E. A., Metcalfe, N., & et al. 2017, ArXiv e-prints

Estrada, J., Alvarez, R., Abbott, T., Annis, J., Bonati, M., Buckley-Geer, E., Campa, J., Cease, H., Chappa, S., DePoy, D., Derylo, G., Diehl, H. T., Flaugher, B., Hao, J., Holland, S., Huffman, D., Karliner, I., Kubik, D., Kuhlmann, S., Kuk, K., Lin, H., Roe, N., Scarpine, V., Schmidt, R., Schultz, K., Shaw, T., Simaitis, V., Spinka, H., Stuermer, W., Tucker, D., Walker, A., & Wester, W. 2010, in Proc. SPIE, Vol. 7735, Ground-based and Airborne Instrumentation for Astronomy III, 77351R

Flaugher, B., Diehl, H. T., Honscheid, K., Abbott, T. M. C., Alvarez, O., Angstadt, R., Annis, J. T., Antonik, M., Ballester, O., Beaufore, L., Bernstein, G. M., Bernstein, R. A., Bigelow, B., Bonati, M., Boprie, D., Brooks, D., Buckley-Geer, E. J., Campa, J., Cardiel-Sas, L., Castander, F. J., Castilla, J., Cease, H., Cela-Ruiz, J. M., Chappa, S., Chi, E., Cooper, C., da Costa, L. N., Dede, E., Derylo, G., DePoy, D. L., de Vicente, J., Doel, P., Drlica-Wagner, A., Eiting, J., Elliott, A. E., Emes, J., Estrada, J., Fausti Neto, A., Finley, D. A., Flores, R., Frieman, J., Gerdes, D., Gladders, M. D., Gregory, B., Gutierrez, G. R., Hao, J., Holland, S. E., Holm, S., Huffman, D., Jackson, C., James, D. J., Jonas, M., Karcher, A., Karliner, I., Kent, S., Kessler, R., Kozlovsky, M., Kron, R. G., Kubik, D., Kuehn, K., Kuhlmann, S., Kuk, K., Lahav, O., Lathrop, A., Lee, J., Levi, M. E., Lewis, P., Li, T. S., Mandrichenko, I., Marshall, J. L., Martinez, G., Merritt, K. W., Miquel, R., Muñoz, F., Neilsen, E. H., Nichol, R. C., Nord, B., Ogando, R., Olsen, J., Palaio, N., Patton, K., Peoples, J., Plazas, A. A., Rauch, J., Reil, K., Rheault, J.-P., Roe, N. A., Rogers, H., Roodman, A., Sanchez, E., Scarpine, V., Schindler, R. H., Schmidt, R., Schmitt, R., Schubnell, M., Schultz, K., Schurter, P., Scott, L., Serrano, S., Shaw, T. M., Smith, R. C., Soares-Santos, M., Stefanik, A., Stuermer, W., Suchyta, E., Sypniewski, A., Tarle, G., Thaler, J., Tighe, R., Tran, C., Tucker, D., Walker, A. R., Wang, G., Watson, M., Weaverdyck, C., Wester, W., Woods, R., Yanny, B., & DES Collaboration. 2015, AJ ,, 150, 150

Flewelling, H. A., Magnier, E. A., Chambers, K. C., Heasley, J. N., Holmberg, C., Huber, M. E., Sweeney, W., Waters, C. Z., Chen, T., Farrow, D., Hasinger, G., Henderson, R., Long, K. S., Metcalfe, N., Nieto-Santisteban, M. A., Norberg, P., Saglia, R. P., Szalay, A., Rest, A., Thakar, A. R., Tonry, J. L., Valenti, J., Werner, S., White, R., Denneau, L., Draper, P. W., Jedicke, R., Kudritzki, R.-P., Price, P. A., Chastel, S., McClean, B., Postman, M., & Shiao, B. 2016, ArXiv e-prints

Gruen, D., Bernstein, G. M., Jarvis, M., Rowe, B., Vikram, V., Plazas, A. A., & Seitz, S. 2015, Journal of Instrumentation, 10, C05032

Hodapp, K. W., Siegmund, W. A., Kaiser, N., Chambers, K. C., Laux, U., Morgan, J., & Mannery, E. 2004, in Proc. SPIE, Vol. 5489, Ground-based Telescopes, ed. J. M. Oschmann, Jr., 667–678

Holland, S., Goldhaber, G., Groom, D., Moses, W., Pennypacker, C., Perlmutter, S., Wang, N., Stover, R., & Wei, M. 1996, in Electron Devices Meeting, IEDM, 911

Holland, S., Groom, D., Palaio, N., Stover, R., & Wei, M. 2003, in IEEE, Vol. 50, IEEE Transactions on Electron Devices, 225

Janesick, J. & Elliott, T. 1992, in Astronomical Society of the Pacific Conference Series, Vol. 23, Astronomical CCD Observing and Reduction Techniques, ed. S. B. Howell, 1

Kaiser, N., Squires, G., & Broadhurst, T. 1995, ApJ ,, 449, 460

Komiyama, Y., Aihara, H., Fujimori, H., Furusawa, H., Kamata, Y., Karoji, H., Kawanomoto, S., Mineo, S., Miyatake, H., Miyazaki, S., Morokuma, T., Nakaya, H., Nariai, K., Obuchi, Y., Okura, Y., Tanaka, Y., Uchida, T., Uraguchi, F., Utsumi, Y., Endo, M., Ezaki, Y., Matsuda, T., Miwa, Y., Yokota, H., Wang, S.-Y., Liaw, E. J., Chen, H.-Y., Chiu, C.-F., & Jeng, D.-Z. 2010, in Proc. SPIE, Vol. 7735, Ground-based and Airborne Instrumentation for Astronomy III, 77353F

Magnier, E. 2006, in The Advanced Maui Optical and Space Surveillance Technologies Conference, E50

Magnier, E. 2007, in Astronomical Society of the Pacific Conference Series, Vol. 364, The Future of Photometric, Spectrophotometric and Polarimetric Standardization, ed. C. Sterken, 153

Magnier, E. A. & Cuillandre, J.-C. 2004, PASP ,, 116, 449

Magnier, E. A., Schlafly, E., Finkbeiner, D., Juric, M., Tonry, J. L., Burgett, W. S., Chambers, K. C., Flewelling, H. A., Kaiser, N., Kudritzki, R.-P., Morgan, J. S., Price, P. A., Sweeney, W. E., & Stubbs, C. W. 2013, ApJS ,, 205, 20

Magnier, E. A., Schlafly, E. F., Finkbeiner, D. P., & et al. 2017, ArXiv e-prints

Magnier, E. A., Schlafly, E. F., Finkbeiner, D. P., Tonry, J. L., Goldman, B., Röser, S., Schilbach, E., Chambers, K. C., Flewelling, H. A., Huber, M. E., Price, P. A., Sweeney, W. E., Waters, C. Z., Denneau, L., Draper, P., Hodapp, K. W., Jedicke, R., Kudritzki, R.-P., Metcalfe, N., Stubbs, C. W., & Wainscoast, R. J. 2016a, ArXiv e-prints

Magnier, E. A., Sweeney, W. E., Chambers, K. C., Flewelling, H. A., Huber, M. E., Price, P. A., Waters, C. Z., Denneau, L., Draper, P., Jedicke, R., Hodapp, K. W., Kudritzki, R.-P., Metcalfe, N., Stubbs, C. W., & Wainscoast, R. J. 2016b, ArXiv e-prints

Onaka, P., Tonry, J. L., Isani, S., Lee, A., Uyeshiro, R., Rae, C., Robertson, L., & Ching, G. 2008, in Proc. SPIE, Vol. 7014, Ground-based and Airborne Instrumentation for Astronomy II, 70140D

Plazas, A. A., Bernstein, G. M., & Sheldon, E. S. 2014, PASP ,, 126, 750

Schlafly, E. F., Finkbeiner, D. P., Jurić, M., Magnier, E. A., Burgett, W. S., Chambers, K. C., Grav, T., Hodapp, K. W., Kaiser, N., Kudritzki, R.-P., Martin, N. F., Morgan, J. S., Price, P. A., Rix, H.-W., Stubbs, C. W., Tonry, J. L., & Wainscoat, R. J. 2012, ApJ ,, 756, 158

Tonry, J. & Onaka, P. 2009, in Advanced Maui Optical and Space Surveillance Technologies Conference, E40

Tonry, J., Onaka, P., Luppino, G., & Isani, S. 2006, in The Advanced Maui Optical and Space Surveillance Technologies Conference, E47

Tonry, J. L., Burke, B. E., Isani, S., Onaka, P. M., & Cooper, M. J. 2008, in Proc. SPIE, Vol. 7021, High Energy, Optical, and Infrared Detectors for Astronomy III, 702105

Tonry, J. L., Stubbs, C. W., Lykke, K. R., Doherty, P., Shivvers, I. S., Burgett, W. S., Chambers, K. C., Hodapp, K. W., Kaiser, N., Kudritzki, R.-P., Magnier, E. A., Morgan, J. S., Price, P. A., & Wainscoat, R. J. 2012, ApJ ,, 750, 99

Wainscoat, R., Weryk, R., Schunova, E., & Carter Chambers, K. 2015, IAU General Assembly, 22, 2251124

Waters, C. Z., Magnier, E. A., Price, P. A., Chambers, K. C., Draper, P., Flewelling, H. A., Hodapp, K. W., Huber, M. E., Jedicke, R., Kaiser, N., Kudritzki, R.-P., Lupton, R. H., Metcalfe, N., Rest, A., Sweeney, W. E., Tonry, J. L., Wainscoat, R. J., Wood-Vasey, W. M., & Builders, P. 2016, ArXiv e-prints